Exploring the electrocatalytic performance of PdIrSnZnMo high entropy alloy (HEA) towards hydrogen evolution reaction in acidic medium: A theoretically supported approach

Rebekah Aruldhas[a*], Praveena Gopalan[b], Daniel Piecha[a,c], Mateusz Szczerba[a,c], Kostiantyn Nikiforow[d] and Grzegorz D. Sulka[a*]

[a]Faculty of Chemistry, Department of Physical Chemistry and Electrochemistry, Jagiellonian University, Gronostajowa 2, 30-387 Krakow, Poland

[b]Department of Physics, PSGR Krishnammal College for Women, Coimbatore, Tamil Nadu, 641004 India

[c]Doctoral School of Exact and Natural Sciences, Jagiellonian University, Lojasiewicza 11, 30-348 Krakow, Poland

[d]Laboratory of Surface Analysis, Institute of Physical Chemistry, Polish Academy of Sciences, Kasprzaka 44/52, 01-224 Warsaw, Poland

[*]*Corresponding author:* sulka@chemia.uj.edu.pl, rebekahgladys@gmail.com

S1. Determination of electrochemical active surface area and turnover frequency

The electrochemical active surface area (ECSA) of electrocatalysts plays a crucial role in enhancing catalytic performance, as it directly correlates with the number of accessible active sites. These sites facilitate the adsorption of reaction intermediates, a key step in hydrogen evolution. Therefore, determining ECSA provides valuable insight into the electrocatalytic efficiency, with higher ECSA values typically associated with improved activity. ECSA was determined from the ratio of the double layer capacitance (C_{dl}) derived from cyclic voltammetry measurements at different scan rates in the non-Faradaic region and the specific capacitance of the electrode (C_S), as presented below:

$$ECSA = \frac{C_{dl}}{C_s}$$

The CV curves recorded at various scan rates for $Pd_{0.01}IrSnZnMo$, $Pd_{0.02}IrSnZnMo$, $Pd_{0.03}IrSnZnMo$, and $Pd_{0.04}IrSnZnMo$ HEAs in the non-Faradaic region (from −0.1 to −0.2 V vs. SCE) are shown in Fig. S1(a-d). In contrast, for the $Pd_{0.05}IrSnZnMo$ HEA catalyst, CV curves were performed in the potential window from 0 to -0.1 V *vs*. SCE (Fig. S1(e)). The adjustment was necessary because a rapid reduction reaction occurred beyond -0.1 V, making the region unstable for ECSA analysis.

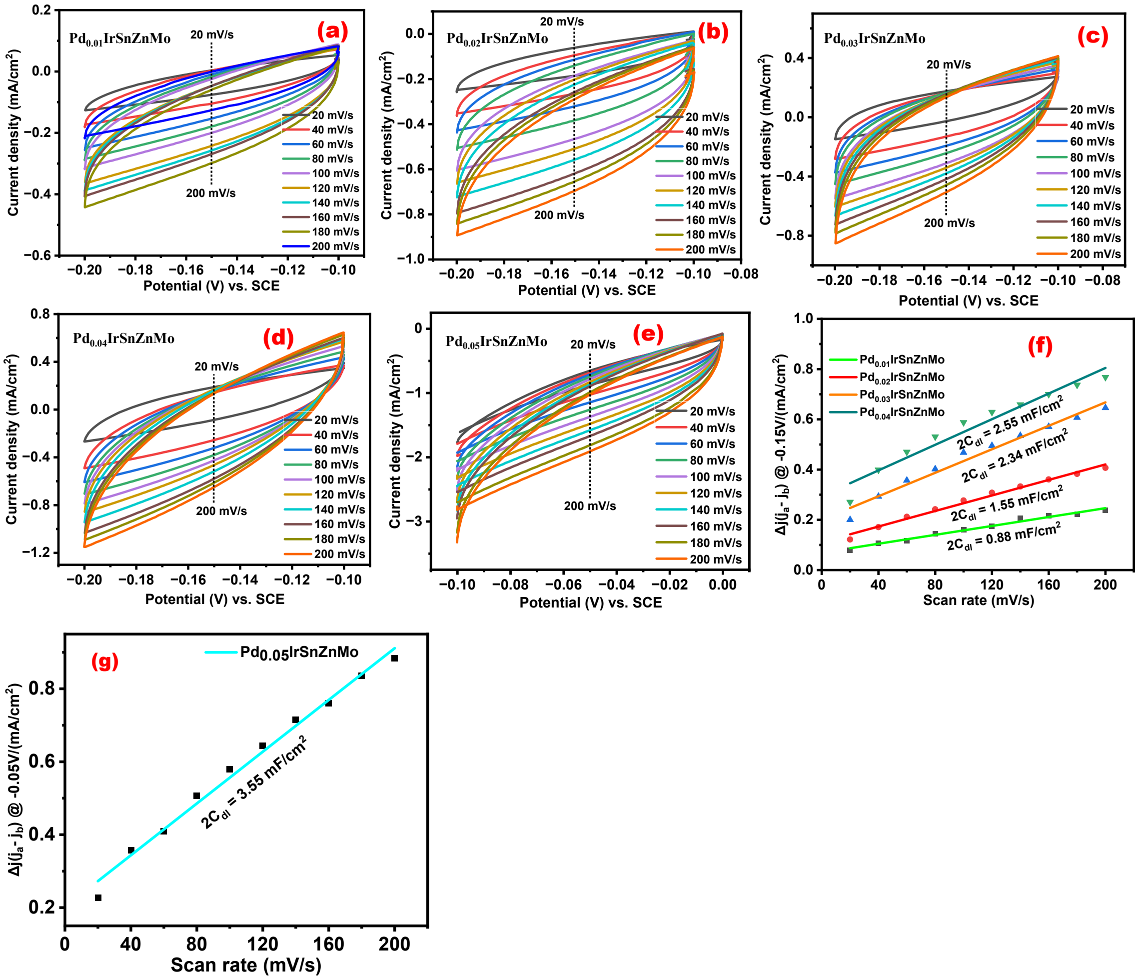

Figure. S1(a-d) CV curves recorded at different scan rates in the non-Faradaic potential region (from -0.1 to -0.2 V *vs.* SCE) for $Pd_{0.01}IrSnZnMo$, $Pd_{0.02}IrSnZnMo$, $Pd_{0.03}IrSnZnMo$, and $Pd_{0.04}IrSnZnMo$ HEAs, (e) CV curves recorded for $Pd_{0.05}IrSnZnMo$ HEA in the non-Faradaic potential region (from 0 to -0.1 V *vs.* SCE), (f) linear fit of the difference between anodic and cathodic current densities at -0.15 V *vs.* SCE as a function of scan rate, and (g) corresponding linear plot for the $Pd_{0.05}IrSnZnMo$ electrocatalyst.

The slope obtained from the linear plots of current density vs. scan rate (Fig. S1(f)) for $Pd_{0.01}IrSnZnMo$, $Pd_{0.02}IrSnZnMo$, $Pd_{0.03}IrSnZnMo$, and $Pd_{0.04}IrSnZnMo$ HEA catalysts corresponds to twice the double-layer capacitance ($2C_{dl}$). The C_S value was assumed to be 40 mF/cm^2, as reported in the literature [23]. The relative ECSA values for $Pd_{0.01}IrSnZnMo$, $Pd_{0.02}IrSnZnMo$, $Pd_{0.03}IrSnZnMo$, $Pd_{0.04}IrSnZnMo$, and $Pd_{0.05}IrSnZnMo$ HEAs are summarized in Table. S1. Among them, $Pd_{0.05}IrSnZnMo$ exhibited the highest ECSA of 4.42 cm^2, significantly larger than those of the other catalysts. This high ECSA indicates a larger number of active sites, which facilitates reaction kinetics by lowering the energy barrier. The roughness factor (R_f), another important parameter characterizing electrocatalytic activity, was calculated as a ratio of ECSA to the geometric area of the electrode (1 cm^2). Accordingly, the R_f values were equivalent to the ECSA values and are also listed in Table. S1.

Table S1. Calculated values of C_{dl}, ECSA, R_f and TOF.

Electrocatalysts	**C_{dl} (mF/cm^2)**	**ECSA (cm^2)**	**R_f**	**TOF (× 10^{-4}/s)**
$Pd_{0.01}IrSnZnMo$	0.44	1.10	1.10	7.69
$Pd_{0.02}IrSnZnMo$	0.77	1.93	1.93	8.02
$Pd_{0.03}IrSnZnMo$	1.175	2.91	2.91	8.36
$Pd_{0.04}IrSnZnMo$	1.275	3.18	3.18	8.69
$Pd_{0.05}IrSnZnMo$	1.77	4.42	4.42	9.02

S2. XPS survey spectra

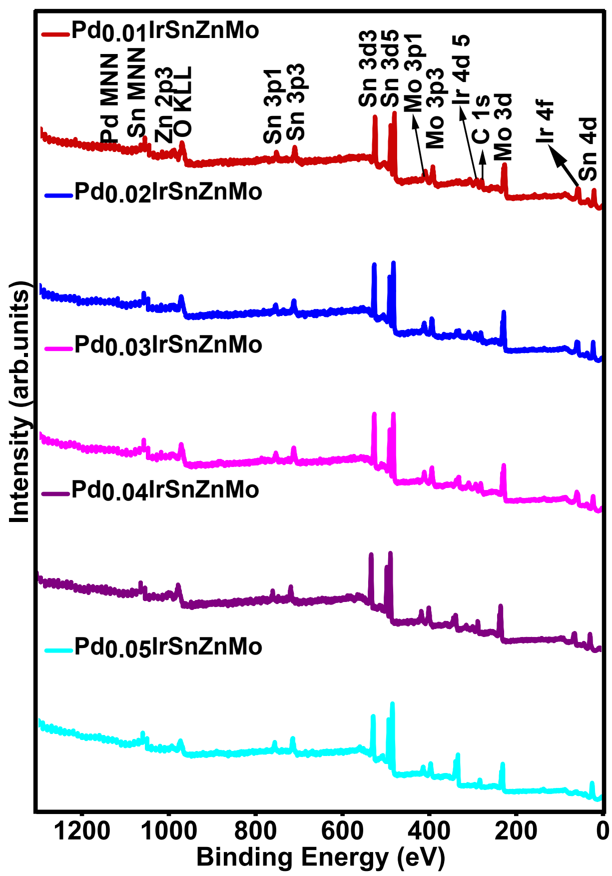

Figure. S2 XPS survey spectra of $Pd_{0.01}IrSnZnMo$, $Pd_{0.02}IrSnZnMo$, $Pd_{0.03}IrSnZnMo$, $Pd_{0.04}IrSnZnMo$, and $Pd_{0.05}IrSnZnMo$ HEAs.

The XPS survey spectra of all HEAs (Fig. S2) confirmed the presence of the constituent elements. This validates the successful alloy formation, with strong bonding among the metallic components leading to a high entropy stabilized single-phase structure.

S3. Elemental analysis

The EDS spectra obtained during HRTEM and FESEM analyses are presented in Fig. S3(a) and (b), respectively. Both spectra confirm the presence of all constituent elements of the PdIrSnZnMo HEA, with no impurities detected. The Cu signal originates from the Cu grid used for sample loading during TEM analysis.

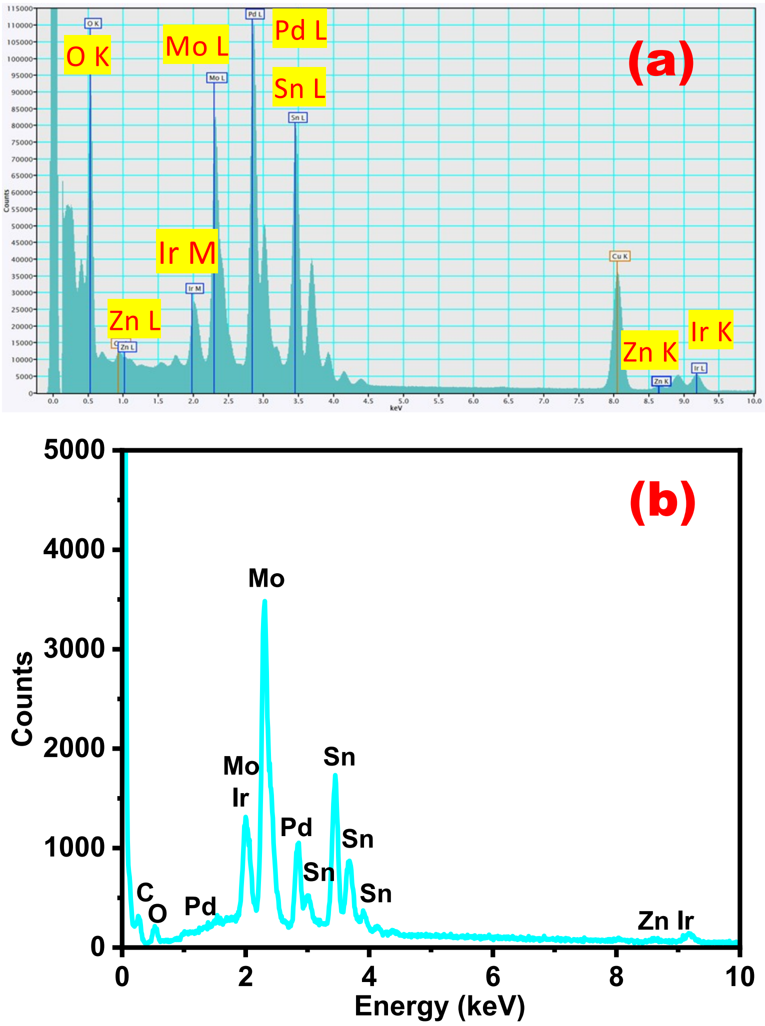

Figure. S3(a) EDS spectrum of $Pd_{0.05}IrSnZnMo$ HEA recorded using STEM, (b) EDS spectrum of $Pd_{0.05}IrSnZnMo$ HEA recorded during FESEM analysis.

Table. S2 Composition of elements (at.%) from ICP-MS analysis.

Elements	0.01 M	0.02 M	0.03 M	0.04 M	0.05 M
Ir	9.0	7.2	6.05	5.03	5.0
Pd	9.6	18.3	20.4	25.1	32.9
Mo	31.6	32.0	34.05	31.08	27.0
Sn	43.8	37.0	34.4	33.3	30.2
Zn	6.0	5.50	5.10	5.54	5.10

S4. DFT calculations

Table. S3 HOMO-LUMO energy gaps and redox potentials for five distinct PdIrSnZnMo conformations optimized at the B3LYP/LANL2DZ level of theory.

Conformers	**$(HOMO)_g$ (eV)**	**$(LUMO)_g$ (eV)**	**$(Energy\ gap)_g$ (eV)**	**$(HOMO)_s$ (eV)**	**$(LUMO)_s$ (eV)**	**$(Energy\ gap)_s$ (eV)**	**Redox Potential (V)**
A	-3.927	-2.067	1.860	-4.043	-2.118	1.925	-0.582
B	-4.906	-3.145	1.761	-3.634	-1.705	1.929	0.342
C	-4.799	-2.895	1.904	-3.326	-1.757	1.568	0.478
D	-4.799	-2.894	1.905	-3.494	-1.913	1.582	0.484
E	-4.933	-2.995	1.938	-3.933	-1.654	2.279	0.299

Table. S4 Total energy, Gibbs free energy, and solvation free energy for five distinct conformations optimized at the B3LYP/LANL2DZ level of theory.

Conformers	**$(HF\ energy)_g$ (a.u)**	**$(Gibbs\ free\ energy)_g$ (a.u)**	**$(HF\ energy)_s$ (a.u)**	**$(Gibbs\ free\ energy)_s$ (a.u)**	**Solvation free energy (kcal/mol)**
A	-367.926	-367.965	-367.945	-367.985	-12.502
B	-367.941	-367.980	-368.004	-368.046	-41.309
C	-367.955	-367.993	-368.000	-368.039	-28.650
D	-367.955	-367.993	-368.000	-368.040	-29.565
E	-367.942	-367.983	-368.014	-368.053	-44.125

Table. S5 Comparison of catalytic performance of outperformed $Pd_{0.05}IrSnZnMo$ HEA with the existing high entropy stabilized Pd-based electrocatalysts in acidic medium.

Catalyst	Current density (mA/cm^2)	Overpotential (mV)	Tafel slope (mV/dec)	Electrolyte	References
PdPtCuNiP high entropy metallic glass (HEMG)	-10	32 and 62	47.4 (1.0 M KOH) and 44.6 (0.5 M H_2SO_4)	1.0 M KOH and 0.5 M H_2SO_4	[1]
IrPdPtRhRu HEA NPs	-10	33.0/17.0 (acidic/alkaline)	-	0.05 M H_2SO_4 and 1M KOH	[2]
Al, Ag, Au, Co, Cu, Fe, Ir, Mo, Ni, Pd, Pt, Rh, Ru, and Ti	-10	32	30.1	0.5 M H_2SO_4	[3]
PdMoGaInNi HEA	-10	13	-179.8	0.5 M H_2SO_4	[4]
PtCuPdAgFe high-entropy intermetallic (PCPAF-HEI) NPs	-10	24	29	0.5 M H_2SO_4	[5]
PtPdRhIrNi (nanoporous nanowires) NPNWs	-10	22	21.6	0.5 M H_2SO_4	[6]
Quinary RhRuPtPdIr HEA thin film	-10	58	42	1 M H_3PO_4 and 0.5 M H_2SO_4	[7]
AuPdFeNiCo HEA	-10	45 (0.5 M H_2SO_4) and 43 (1 M KOH)	32 (acidic medium), 55 (alkaline medium)	0.5 M H_2SO_4 and 1 M KOH	[8]
IrPdPtRhRu HEA	-10	16, 28, and 12 mV in 1.0 M KOH, 1.0 M KOH + 0.5 M NaCl, and 0.5 M H_2SO_4 respectively	31 (1.0 M KOH)	1.0 M KOH, 1.0 M KOH + 0.5 M NaCl, 0.5 M H_2SO_4	[9]
(Ce)-tailored PdCeMoCuRu HEA	-10	12.8	30.4	0.5 M H_2SO_4	[10]
high-entropy MG PdPtCuNiP	-10	35.4	34.2	0.5 M H_2SO_4	[11]
$Pd_{0.05}IrSnZnMo$ HEA	-10	17	52.7	0.5 M H_2SO_4	This work

References

1. Zhe Jia, Keita Nomoto, Qing Wang, Charlie Kong, Ligang Sun, Lai-Chang Zhang, Shun-Xing Liang, Jian Lu, and Jamie J. Kruzic, A self-supported high-entropy metallic glass with a nanosponge architecture for efficient hydrogen evolution under alkaline and acidic conditions, Advanced Functional Materials 31 (2021) 2101586.
2. Dongshuang Wu, Kohei Kusada, Tomokazu Yamamoto, Takaaki Toriyama, Syo Matsumura, Ibrahima Gueye, Okkyun Seo, Jaemyung Kim, Satoshi Hiroi, Osami Sakata, Shogo Kawaguchi, Yoshiki Kubota and Hiroshi Kitagawa, On the electronic structure and hydrogen evolution reaction activity of platinum group metal-based high-entropy-alloy nanoparticles, Chemical Science 11 (2020) 12731.
3. Ze-Xing Cai, Hiromi Goou, Yoshikazu Ito, Tomoharu Tokunaga, Masahiro Miyauchi, Hideki Abe and Takeshi Fujita, Nanoporous ultra-high-entropy alloys containing fourteen elements for water splitting electrocatalysis, Chemical Science 12 (2021) 11306.
4. Xianbiao Fu, Jiahao Zhang, Shaoqi Zhan, Fanjie Xia, Chengjie Wang, Dongsheng Ma, Qin Yue, Jinsong Wu, and Yijin Kang, High-entropy alloy nanosheets for fine-tuning hydrogen evolution, ACS Catalysis 12 (2022) 11955−11959.
5. Shaohui Zheng, Jiuyi Hu, Ri Feng, Jiayu Xu, Yingjie Yu, Linpo Li, Wenjing Liu, Weina Zhang, Fengwei Huo, and Faisal Saleem, Ultrathin template approach to synthesize high-entropy intermetallic nanoparticles for hydrogen evolution reaction, Small Structures 5 (2024) 2300537.
6. Ying Wang, Bin Yu, Ming He, Zhihua Zhai, Kuibo Yin, Fangong Kong, and Zhonghua Zhang, Eutectic-derived high-entropy nanoporous nanowires for efficient and stable water-to-hydrogen conversion**,** Nano Research 15 (2022) 4820–4826.
7. Lin Jing, Yiming Zou, Ronn Goei, Leyan Wang, Jiamin Amanda Ong, Anatoli Kurkin, Yun Li, Kwan W. Tan, and Alfred Iing Yoong Tok, Conformal noble metal high-entropy alloy nanofilms by atomic layer deposition for an enhanced hydrogen evolution reaction, Langmuir 39 (2023) 3142−3150.
8. Sangmin Jeong, Anthony J. Branco, Silas W. Bollen, Connor S. Sullivan and Michael B. Ross, Universal pH electrocatalytic hydrogen evolution with Au-based high entropy alloys, Nanoscale 16 (2024) 11530.
9. Yingjie Yu, Qi Wang, Xiaohan Li, Qiao Xie, Ke Xu, Shaowei Zhang, Haijun Zhang, Mingxing Gong, Wen Lei, Laser-thermal reduction synthesis of high-entropy alloys towards high-performance pH universal hydrogen evolution reaction, Nano Materials Science 7 (2025) 400-408.
10. Yujia Zhang, Kunkun Nie, Binjie Li, Lixin Yi, Chen Hu, Ziyi Wang, Xiaorong Hao, Wenlin Zhang b, Zhengqing Liu, Wei Huang, Cerium-optimized platinum-free high-entropy alloy nanoclusters for enhanced ampere-level sustainable hydrogen generation, Applied Catalysis B: Environment and Energy 360 (2025) 124529.
11. Yangzheng Li, Junlei Tang, Hailong Zhang, Yingying Wang, Bing Lin, Jichao Qiao, Hongpeng Zheng, Zongxue Yu, Yiding Liu, Taigang Zhou, Xianzhang Lei, In-situ construction and repair of high catalytic activity interface on corrosion-resistant high-entropy amorphous alloy electrode for hydrogen

production in high-temperature dilute sulfuric acid electrolysis, Chemical Engineering Journal 453 (2023) 139905.